Geomorphology 455 (2024) 109176

Contents lists available at ScienceDirect

Geomorphology

journal homepage: www.journals.elsevier.com/geomorphology

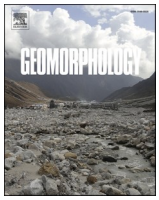

Sediment connectivity as a key to understand geomorphic effects of the Storm Alex in two mountain catchments of the Mediterranean Alps (Italy)

Francesca Ardizzone [a], Giuseppe Esposito [a,*], Marco Cavalli [b], Stefano Crema [b], Federica Fiorucci [a]

[a] National Research Council – Research Institute for Geo-hydrological Protection (CNR-IRPI), Via della Madonna Alta 126, 06128 Perugia, Italy
[b] National Research Council – Research Institute for Geo-hydrological Protection (CNR-IRPI), Corso Stati Uniti 4, 35127 Padova, Italy

ARTICLE INFO

Keywords:
Rainstorm
Mountain catchment
Landslide
Inventory map
Index of connectivity
Sediment transfer

ABSTRACT

The occurrence of extreme rainfall events over mountain catchments is likely to trigger mass failure processes on hillslopes and sediment transport within the channel network. Understanding the degree of linkage between the sediment sources and transfer pathways downstream is essential in those catchments where settlements are affected by hydro-geomorphic processes, in order to plan suitable interventions for risk mitigation. A recent storm (October 2020) named "Alex", estimated to be an extratropical cyclone with a more than 100-year return period, hit the Mediterranean Alps at the border between Italy and France, triggering deadly landslides and flooding processes. This work focuses on two adjacent mountain catchments located in the Liguria region (Italy) which share the same outlet, where a small village was damaged by high-magnitude sediment transport and deposition processes during the storm. In order to analyze sediment dynamics at the catchment scale leading to severe damage to the urban settlements at the outlet, an integrated approach was used. Very high resolution (0.5 m) satellite imagery was employed to map the mass failure processes on the hillslopes with a visual interpretation. This dataset was then compared with a map of the Index of Connectivity created using the SedInConnect 2.3 software to characterize the pre-event structural connectivity in both catchments. The integration of these two datasets permitted understanding that debris slides evolving into debris flows downstream supplied most of the sediments to the channel network. These processes concentrated mainly in a specific catchment where hillslopes have the highest connectivity with the valley bottom. This outcome provided a clear evidence that inventory maps developed soon after an extreme event, coupled with sediment connectivity datasets, can provide relevant information for future land management and risk mitigation strategies. These can be exploited to prioritize structural interventions in specific areas, to reduce the connectivity or disconnect inhabited areas from the hydro-geomorphic systems and avoid future damage.

1. Introduction

Mountain catchments represent very sensitive geomorphic systems and may be regarded as a sentinel of change when considering climatic variability. Abundant and intense rainfall can trigger erosion processes, landslides and debris flows transferring large amounts of sediment and wood from low-order streams and adjacent hillslopes to the main channel network (Stoffel et al., 2014; Borga et al., 2014; Peng et al., 2015; Handwerger et al., 2019; Bookhagen, 2010). The study of geomorphic processes and their transfer pathways emphasizes the significance of sediment connectivity. Having a clear understanding of connectivity is crucial to comprehending the behavior of hydro-geomorphic systems (Cavalli et al., 2019). Essentially, connectivity is an emergent property and refers to the level of linkage between different components of a system (Fryirs, 2013; Heckmann et al., 2018). Indices of sediment connectivity (Borselli et al., 2008; Cavalli et al., 2013; Heckmann et al., 2018) serve as effective tools for analyzing the sediment transfer through catchment compartments, by providing information on the potential coupling/decoupling patterns between sediment sources and targets of interest (e.g., channels, lakes, road network), as well as a general understanding of the sediment cascade and sediment transport pathways (Burt and Allison, 2010).

In a given catchment, the sediment connectivity varies over time and space, especially after infrequent, high-magnitude rainfall events

* Corresponding author.
E-mail address: giuseppe.esposito@irpi.cnr.it (G. Esposito).

https://doi.org/10.1016/j.geomorph.2024.109176
Received 26 July 2023; Received in revised form 1 March 2024; Accepted 22 March 2024
Available online 23 March 2024

(Bracken et al., 2015) which may provide high energy inputs resulting in a significant sediment delivery able to change the geomorphic coupling among different sectors of the catchment with respect to a selected target (Bertoldi et al., 2010; Surian et al., 2016; Pellegrini et al., 2021; Scorpio et al., 2022). In 2002, Harvey presented examples of coupling mechanisms at different spatial scales, from local (e.g. hillslope-to-channel and reach-to-reach coupling) to large (zonal and regional coupling), highlighting that the coupling influences the geomorphological evolution of a system (Harvey, 2002). This author found that as the spatial scale changes, the relevancy of the controlling factors changes; at local scale the climatic factor seems to dominate, but increasing the scale towards zonal and regional, the tectonic and the geomorphic history assume more relevance. In fact, on a local scale the significant timescales are essentially due to the frequency of events and the recovery time. At larger scales the propagation time becomes relevant. Forms of disconnectivity such as "buffer", "barriers" and "blankets" are demonstrated to influence the strenght of coupling (Fryirs et al., 2007). The degree of sediment flux connection or disconnection depends on both properties of processes (i.e. functional connectivity - Wainwright et al., 2011) and on catchment morphology in terms of types and spatial distribution of landforms and man-made structures, as addressed by the structural connectivity (Fryirs et al., 2007; Cavalli et al., 2019). The latter, in fact, depends on the intrinsic properties of a catchment (e.g., topography, slope roughness, material properties) which control the physical linkages among the different spatial units with reference to sediment transport (Keesstra et al., 2018; Heckmann et al., 2018; Najafi et al., 2021). Structural connectivity can provide valuable indications about the possible sediment pathways at the catchment scale, demonstrating a predictive (or explanatory) capability (Cucchiaro et al., 2019; Martini et al., 2022). Indices of connectivity, which are mainly devised to semi-quantitatively investigate the structural connectivity, may provide useful information by indicating, for example, if a slope covered by erodible sediments is structurally connected to a valley bottom, or if a low-order channel is capable or not to supply sediment into the main stream. On the other hand, after a high-magnitude event, an accurate mapping of the occurred processes can be used to assess whether areas considered structurally connected are also functionally connected, as well as if the recent sediment transport has modified the connectivity pathways and the consequent rates of transfer. This may provide useful information for updating the structural status of the analyzed catchment, being a function of frequency–magnitude–duration and thresholds of the processes/events (Singh et al., 2021).

Sediment connectivity indices can be used as tools for a wide range of management issues, and for targeting specific actions (Fressard and Cossart, 2019). Heckmann et al. (2018) pointed out the use of sediment connectivity to identify, rank and prioritize strategies in catchment management, as well as in decision-support systems for the

Fig. 1. Location map of the study area (white polygons) showing the rain gauges (light blue triangles) used in this study. Some representative localities are also indicated.

Table 1
Topography, land cover and lithological characteristics of the catchments.

Topography	West catchment		East catchment	
Area (km^2)	14.4		11.5	
Slope range (°)	75.4		75.1	
Slope average (°)	31.5		31.8	
Elevation min (m)	438		438	
Elevation max (m)	2152		1846	
Relief (m)	1714		1408	
Total stream length (km)	82		73.8	
Drainage density	5.7		6.4	
LAND COVER	**(km^2)**	**%**	**(km^2)**	**%**
Woodland	11.15	77	8.38	73
Rangeland	3	21	2.96	25
Urban/bare soil	0.31	2	0.21	2
LITHOLOGY	**(km^2)**	**%**	**(km^2)**	**%**
Carbonate rocks	0.47	3	0.3	3
Mixed sedimentary rocks	1.71	12	2.8	24
Siliciclastic sedimentary rocks	12.05	84	7.6	66
Unconsolidated clastic rocks	0.21	1	0.8	7

identification and possible prioritization of critical sediment source areas. For this purpose, many authors focused their analyses on the interaction between sediment source areas and structural connectivity, to characterize their degree of coupling with the channel network or possible anthropic settlements (Cavalli et al., 2016; Surian et al., 2016; Tiranti et al., 2018; Rainato et al., 2017). Persichillo et al. (2018), for example, evaluated how anthropogenic modifications to the landscape influenced sediment delivery associated with shallow landslides, verifying that many source areas (i.e. landslides) were highly connected with roads and inhabited areas downstream thus requiring risk mitigation measures. In case of extreme rainfall events resulting in widespread geo-hydrological processes over multiple catchments, or over multiple locations within the same catchment, the detection and mapping of processes combined with connectivity assessment can be useful to select areas to which remediation interventions should be realized first, to mitigate residual risk conditions (e.g., Pellegrini et al., 2021).

Maps of the Index of connectivity (IC) are also coupled with landslide susceptibility models to predict the potential sediment sources that could affect settlements and infrastructure. For example, Bordoni et al. (2018) estimated landslide-prone road sections including the IC in a data-driven landslide model. Cislaghi and Bischetti (2019) integrated landslide susceptibility and total travel distance of sediment deposit for estimating a process-based sediment connectivity by developing a physical-based model for assessing the probability of failure, and a statistical-empirical procedure for estimating the in-channel sediment yield.

Advanced remote sensing techniques provide relevant support in detecting sediment source areas in the ex-post phase of large infrequent events, as well as in characterizing their magnitude and spatial distribution. High-resolution topography (HRT) developed from spaceborne and airborne platforms coupled to change detection operations are being increasingly used (Passalacqua et al., 2015). HRT datasets were successfully employed to develop landslides and debris flow inventories (Guzzetti et al., 2012 and references therein; Murillo-García et al., 2015), and to analyze sediment connectivity at the catchment scale, as extensively documented in the Italian Alps (Cavalli et al., 2013; Cucchiaro et al., 2019; Schopper et al., 2019; Buter et al., 2022; Pellegrini et al., 2021; Martini et al., 2022; Scorpio et al., 2022). For example, Yan et al. (2022) mapped the landslides occurred during a rainstorm by means of fieldwork and unmanned aerial vehicle techniques and calculated the amount of soil erosion to explore the relationship between sediment connectivity of landslides and sediment yield of slope-channel cascades.

In the current study, Very High Resolution (VHR) satellite imagery (i.e., with ground sample distance ~1.0 m according to https://earth.esa.

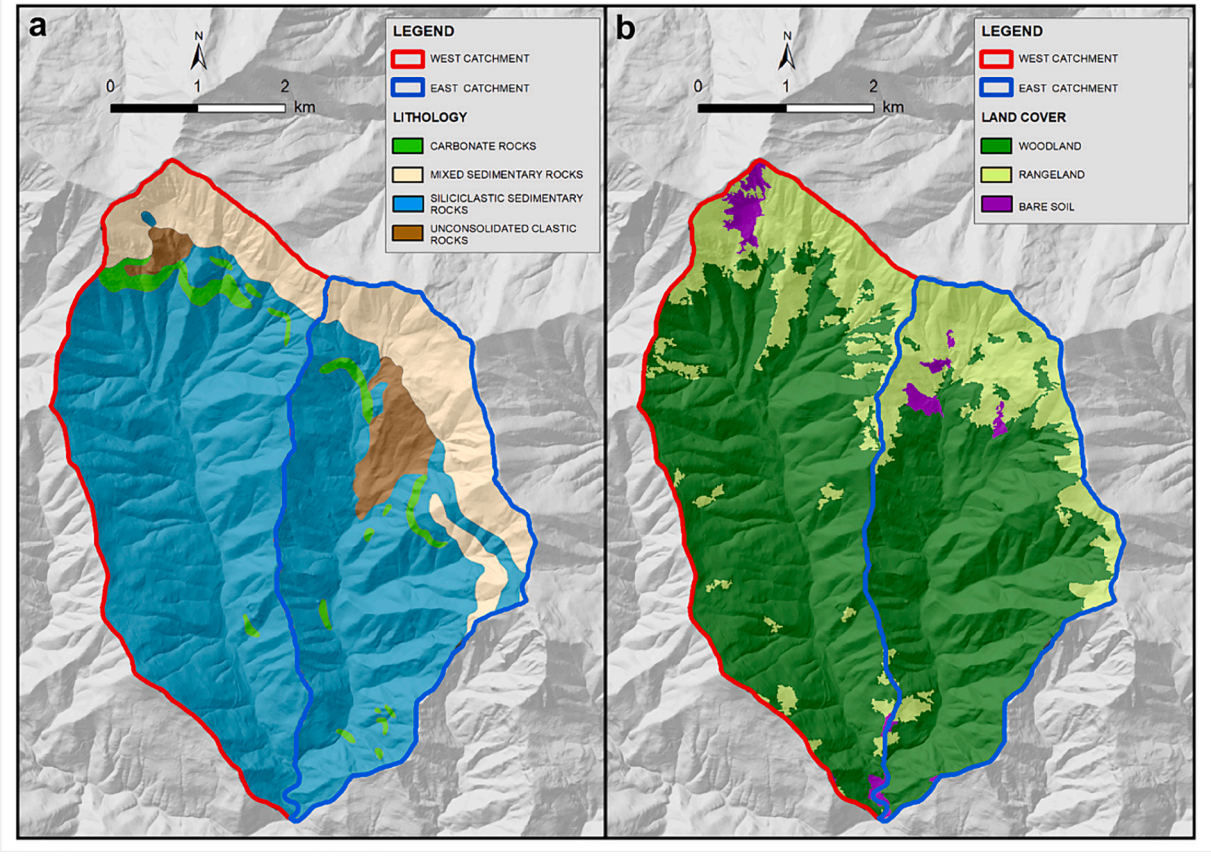

Fig. 2. Lithology and land cover of the study catchments.

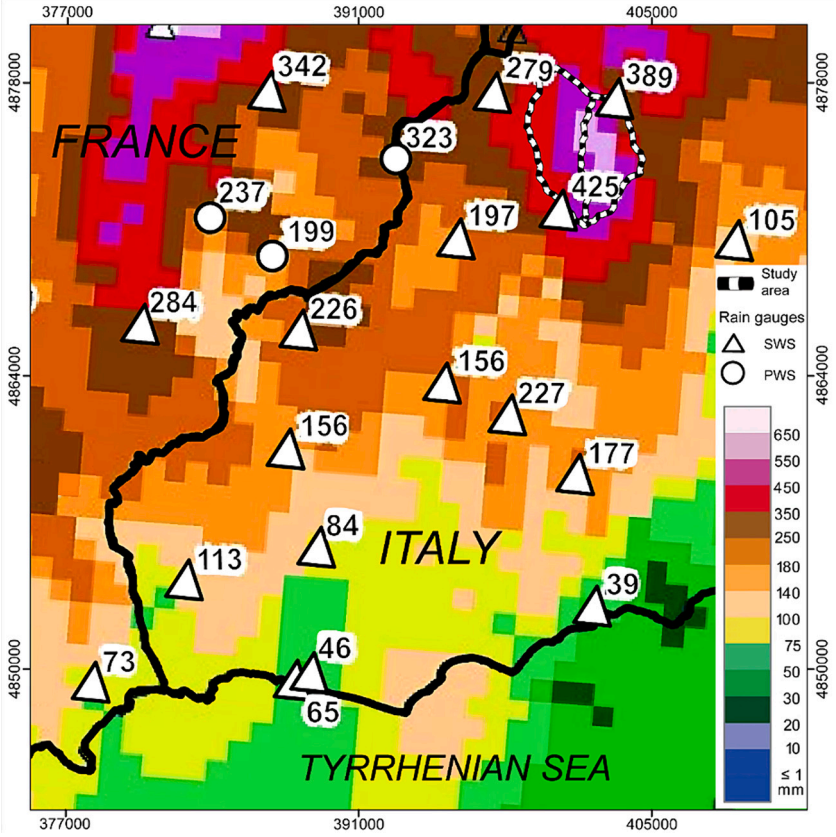

Fig. 3. 24-h rainfall accumulation from ANTILOPE, reanalyzed between 06 a.m. UTC on 02 October 2020 and 06 a.m. UTC on 03 October 2020. The dashed line indicates the study area; the white triangles show the SWS rain gauges; the white circles show the PWS rain gauges. Modified by Chochon et al. (2022).

int/eogateway/activities/edap/vhr-hr-mr-optical-missions) was exploited to develop a detailed inventory of rainfall-induced hillslope instability processes in two adjacent mountain catchments of the Liguria Region (northern Italy), which were impacted by the storm Alex in 2020 (Chmiel et al., 2022). In addition, a geomorphological inventory map was prepared according to the methods explained by Bucci et al. (2021) and Ardizzone et al. (2023) to investigate the pre-existing landslides. The areas affected by the inventoried events were then overlayed to a map of the Index of Connectivity (IC), as proposed by Cavalli et al. (2013), to understand: i) the effect of pre-event structural connectivity on different types of mass movements triggered by the extreme event; ii) which sediment sources were most connected to the valley bottoms (target) where high-magnitude sediment transport took place; iii) spatial relationships between the landslides triggered by the storm Alex and the pre-existing landslides, as well as the patterns of connectivity in the landslide overlapping areas and outside.

2. Study area and storm Alex description

The study area is in western Liguria (Italy) (Fig. 1), at 3 km from the French border, and extends for about 26 km^2. The area includes the Capriolo and Corte mountain catchments, namely west and east catchments, that extend for 14.4 and 11.5 km^2 respectively (Fig. 1). Both catchments share a common outlet located at the confluence with the Argentina valley, in the Molini di Triora village. The Frontè Mount represents the highest elevation (2152 m a. s. l.), and the outlet at the Molini di Triora village is the lowest one (438 m a. s. l.). Table 1 reports the main characteristics of the two catchments.

The lithological map of Italy (Bucci et al., 2022) reveals that four main lithological classes are present in the study area, in different proportions varying within the two catchments (Fig. 2 and Table 1): i) siliciclastic sedimentary rocks; ii) mixed sedimentary rocks; iii) carbonate rocks; iv) unconsolidated clastic rocks.

In addition, debris related to landslides and eluvium-colluvium deposits is present, together with landslides represented mostly by debris slides and rock falls.

The land cover is mainly represented by woodland, rangeland, and urban area/bare soil in similar proportions within the two catchments (Fig. 2 and Table 1).

The climate is characterized by low amounts of rainfall in the summer and medium-high precipitations in the winter, with average annual values up to 1200 mm. The area is also affected by extreme events of precipitation both in frequency and magnitude (https://www.mite.gov.it/sites/default/files/archivio/allegati/clima/pnacc_allegato_1.pdf). In fact, between 1 and 3 October 2020, a particularly severe storm named "Alex" hit the Mediterranean Alps along north-western Italy and southern France regions (Chmiel et al., 2022; Prakash and Manconi, 2021). According to Yassine et al. (2022), the storm Alex was estimated to be a more than 100-year return period event, with typical characteristics of extratropical cyclones (Ginesta et al., 2023).

The associated rainfall fell in the Liguria region from 7:00 p.m. of 1 October to 1:00 p.m. of 3 October.

According to the data measured by rain gauges of the ARPAL network (Fig. 1), between 06 a.m. UTC on 02 October 2020 and 06 a.m. UTC on 03 October 2020, rainfall in the study area increased progressively towards the eastern direction, reaching the maximum 24-H accumulation of 425 mm at the Triora station. For the same time span, the Verdeggia and Poggio Fearza rain gauges recorded rainfall amounts of 279 and 389 mm respectively. In addition, the ANTILOPE reanalyzed product shown in Fig. 3, and available from Chochon et al. (2022), indicated 24-H cumulated rainfall of more than 500 mm in correspondence of the east catchment.

The storm triggered devastating flash floods and landslides, causing damage to electrical, water and sewage networks and partial collapse of

infrastructures, resulting in the isolation of numerous localities (Technical report about the hydro-meteorological event of 1–3 October 2020 developed by the regional Environmental Protection Agency of the Liguria Region, https://www.arpal.liguria.it/). The village of Molini di Triora was affected by severe damage due to sediment transport and deposition, in a way that many buildings and vehicles were inundated by mud and debris, and both electrical power and drinking water networks were interrupted for several days. The economic impact was estimated at € 13 million, whereas no consequences resulted for people.

The event was also characterized by high winds and storm surges that caused widespread damage along the coast.

3. Methodology

3.1. Inventory of the hillslope instability processes

We used post-event GeoEye imagery to perform a monoscopic visual interpretation aimed at identifying sharp evidence of hillslope instability processes triggered by the storm Alex. The images were acquired on 20 October 2020, and provided in GeoTIFF format.

Pre-processing of the raw data was carried out with the ERDAS IMAGINE software, and consisted of the following steps: 1) pansharpening; 2) orthorectification; 3) normalized difference vegetation index (NDVI) calculation. Pansharpening was carried out to combine higher resolution panchromatic (0.5 m) and lower resolution multispectral information (2 m) to obtain high-resolution color images. To do this, we used the Resolution Merge algorithm included in ERDAS IMAGINE.

The orthorectification was based on a series of ground control points (GCPs) derived from georeferenced products, such as orthophotographs "AGEA 2016" available as WMS service (https://geoportal.regione.liguria.it/catalogo/mappe.html) in the UTM-ETRF2000 coordinate system, zone 32 N, with a pixel size of 20 cm. The GCPs were chosen in GIS environment among reference points represented by natural or anthropic objects clearly visible in the orthophotographs (e.g., road crossings, soccer field corners, boulders), which were stable both in space and through time. Together with GCPs, we also used as support the Tinitaly DTM with a pixel size of 10 m and projection EPSG 32632, provided by the National Institute of Geophysics and Volcanology (Tarquini et al., 2023).

Table 2
Weighting factors.

Land cover	W
woodland	0.6
rangeland	0.83
bare soil	0.95

Because of a rough morphology, the study area was affected by widespread shadow effects in the GeoEye imagery. In order to overcome this drawback, a NDVI layer was developed with ERDAS IMAGINE from each GeoEye image. In fact, the NDVI spectral index allows a straightforward identification of the bare terrain also left by slope failures with respect to vegetated surrounding areas (Fig. 4), and provides relevant support to facilitate trained investigators in recognizing and mapping landforms in shadowed areas, as explained by Fiorucci et al. (2019). Both NDVI and pansharpened color images were loaded in ArcGIS® software, version 10.7, to identify sharp evidence of mass movements based on common criteria adopted by geomorphologists (Fiorucci et al., 2011 and references therein). The comparison between the GeoEye imagery with the available pre-event data, such as orthophotographs "AGEA 2016" and images acquired by the "Sentinel-2" satellite platform on 13 September 2020 (10 m/pixel), supported the accurate identification of mass movements triggered by the storm Alex. The Sentinel-2 post-event image, acquired on 8 October 2020, was also used to confirm the temporal relationship of mass movements with the storm Alex, by assessing the associated radiometric changes (i.e., pre- and post-event as shown in Fig. 4).

Each landform was represented with a polygon identified with a unique incremental ID number. Landforms associated to water erosion were classified as "channelized flow erosion" as they were recognized in the form of incision within the first-order drainage channels. Landslides instead were classified according to the classification of Cruden and Varnes (1996) in "debris slide", and "debris slide/debris flow" where the

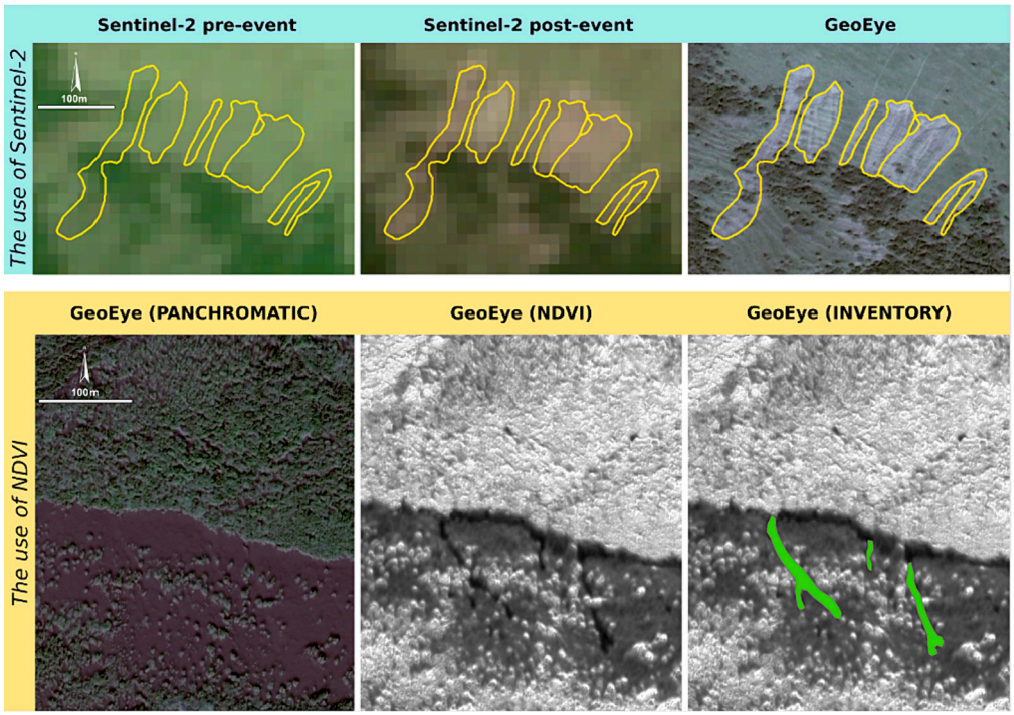

Fig. 4. Examples of the use of Sentinel-2 imagery and GeoEye-derived NDVI products to recognize mass movements related to the storm Alex.

initial slide movement transitioned into a flow downstream.

For each polygon, the elongation parameter was calculated with ArcGis from the ratio of the length to the width of the minimum bounding rectangle that has sides along the orientation of the polygon.

3.2. Geomorphological inventory map

A geomorphological inventory shows the cumulative effects of many landslide events over a period of tens, hundreds or thousands of years (e.g., Cardinali et al., 2001; Galli et al., 2008). In a geomorphological inventory, the age of the landslides is not differentiated, or is given in relative terms i.e., recent, old or very old. The geomorphological inventory map was prepared by means of the visual interpretation of three sets of digital stereoscopic aerial photographs acquired in 1974, 1990 and 1994 (freely available at the website of the Liguria Region Authority: https://geoportal.regione.liguria.it/servizi/fototeca.html). The digital aerial photographs were interpreted by using the freeware StereoPhoto Maker (SPM, http://stereo.jpn.org/eng/stphmkr/) that allows for the anaglyph view of stereo-pairs (Bucci et al., 2021). The geomorphological information was directly drawn on a digital topography by using ArcGis. Such a topography consisted of the 5 m DTM of the Liguria Region Authority obtained from the previously cited geoportal.

3.3. Sediment connectivity calculation

To assess the structural connectivity in the two catchments under investigation, we applied the geomorphometric index IC. This index primarily aims to establish the link in terms of sediment connectivity between various parts of the catchment, such as hillslopes and key features like the catchment outlet, main channel network, or a specific cross-section along the channel. The IC can be defined as the logarithm of the ratio between two components - an upslope and a downslope component. The upslope component expresses the potential for sediment available upslope to be routed downward, while the downslope component indicates the length of the sediment flux path to the nearest sink or target. Both components of IC include a weighting factor (W) to represent the impedance to runoff and sediment fluxes that may be based on land use (e.g., Borselli et al., 2008; Persichillo et al., 2018; Martini et al., 2019; Zanandrea et al., 2020) or surface roughness characteristics (e.g. Cavalli et al., 2013; Trevisani and Cavalli, 2016). Further information about IC can be found in Cavalli et al. (2013).

IC maps of the two analyzed catchments were created by using SedInConnect 2.3 software (Crema and Cavalli, 2018). The required input data consisted of: a) DTM; b) map of the weighting factor; and c) a polygon of the selected target. In this study, the 5 m DTM of the Liguria Region Authority was used. It was hydrologically corrected with the TauDEM ArcGIS toolbox (http://hydrology.usu.edu/taudem/taudem5/index.html) for removing local depressions. The weighting factor (W) was developed by starting from the land cover map derived from the GeoEye imagery. Specifically, the latter was obtained in ArcGIS with a supervised maximum likelihood classification of each image, by selecting a series of land cover categories. Following the approach by Persichillo et al. (2018), each category was associated to a W factor that was derived in turn from a Manning's roughness value (n). Specifically, the following equation was employed:

$$W = 1 - n$$

For each land cover type, the value of W is insicated in Table 2.

The valley bottoms of the two catchments were selected as targets to investigate their potential connection with sediments derived from the sediment sources on the hillslopes (i.e, the mapped instabilities), which were then delivered through the main channel network to the urban center of Molini di Triora located in correspondence of the outlet downstream. In this way the analysis was focused exclusively on lateral connectivity and thus on hillslope-to-channel coupling, to better understand the different sediment sources behavior without the bias due to the distance to the outlet. The valley bottoms were defined in ArcGIS by applying the flow direction and accumulation tools to the 5 m DTM, and a buffer of 25 m to the extracted drainage network.

4. Results

4.1. Event inventory map and sediment connectivity

The inventory of mass failures on the hillslopes developed from visual interpretation of the GeoEye imagery consists of 214 debris slides (DS), 79 debris slides/debris flows (DS/DF), and 9 zones affected by channelized flow erosion (CFE). All the polygons associated to the recognized processes are shown in Fig. 5, whereas the total frequency and affected area calculated for each catchment are reported in Table 3. Generally, the numbers of debris slides are similar in the two catchments, whereas those related to the other processes are rather different. In fact, the number of DS/DF is more than twice in the east catchment, whereas channels affected by CFE occur mostly in the west catchment. Besides the frequency of processes, the east catchment is that with the highest surface affected by mass movements (296,019 $\pm$ 2916 m^2) with respect to the western one (127,264 $\pm$ 1170 m^2). Noteworthy is the area affected by debris slides/debris flows in the east catchment, evaluated to 177,443 m^2. A visual assessment of the map in Fig. 5 reveals that the spatial distribution of the inventoried processes is also different within the two catchments. In the western one, they concentrate upstream, whereas in the eastern one they are more widespread.

Part of the sediments mobilized by the described processes throughout the two catchments reached the outlet in the Molini di Triora village (Fig. 5). VHR spaceborne images related to this area, acquired before and after the storm Alex, are shown in Fig. 6. A general overview of the post-event image reveals the relevant amount of sediments deposited in the valley bottom, also within inhabited zones. Besides deposition, landslides and local undercutting of the slopes also affected this sector, as depicted in the two photographs collected on the ground.

The spatial distribution of the mapped instability processes was investigated with respect to both land cover and lithology characterizing the two catchments. With regard to the land cover, data in Fig. 7 and Table 4 show that the highest concentration of DS and DS/DF occurs in the rangeland category, whereas the CFE prevails on bare soil. In the latter land cover category, DS and DS/DF are also considerable, whereas lower amounts occur in the wooded area, except for DS in the east catchment. The spatial distribution with respect to lithology (Fig. 7 and Table 4) shows that, generally, there is a concentration of DS in areas characterized by carbonate rocks, whereas DS/DF and zones affected by CFE occur mostly in areas with mixed sedimentary rocks. In unconsolidated clastic rocks, however, a considerable occurrence of both DS and DS/DF can be also identified.

The IC map of the study catchments is reported in Fig. 8, whereas statistics are shown in Table 5. Generally, the latter shows very similar values with no particular differences between the two catchments. On the other hand, the IC map shows a pattern characterized by IC values increasing towards the valley bottoms selected as target. This behavior is common within IC maps since the sediment connectivity is higher in correspondence with the targets due to the shorter paths the sediment has to travel to reach them.

More specifically, the sediment connectivity analysis emphasizes the different degrees of connection of the hillslopes and heads of the two catchments. The hillslopes on the western margin of the east catchment are characterized by a higher connectivity with respect to the opposite hillslopes that present a quite larger number of mapped instability processes. All the hillslopes of the west catchment are more homogeneous in terms of sediment connectivity patterns. Catchment heads clearly differ, with the head of the east one that is more effectively connected to the main stream channel and is, not surprisingly, more affected by channelized processes with a quite long runout. A generally lower connection can be observed in the head of the west catchment.

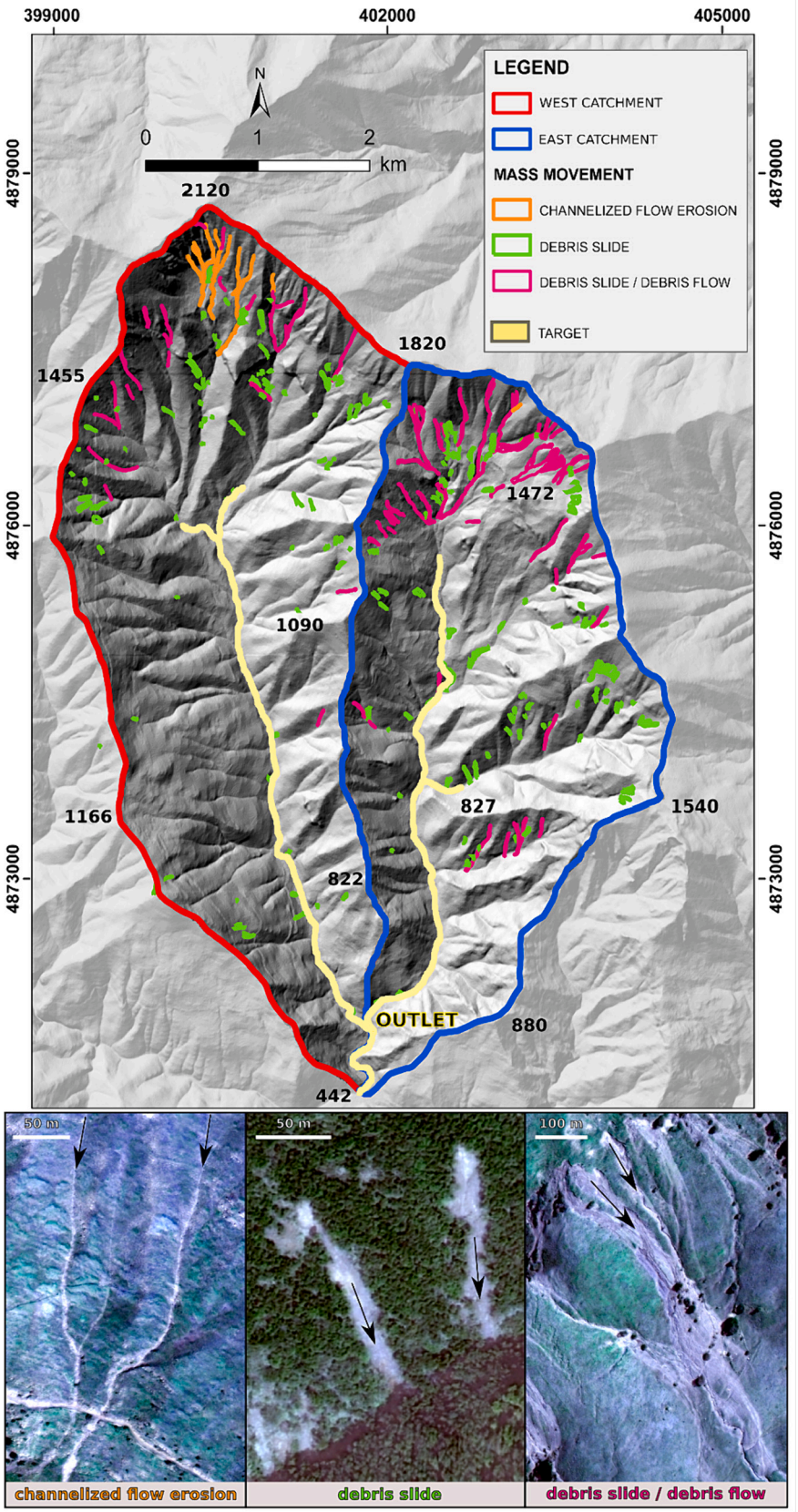

Fig. 5. Inventory map developed from interpretation of the GeoEye imagery. The pictures below show examples of the identified processes.

Table 3
Frequency and area of the hillslope instability processes for each catchment.

Process	West catchment		East catchment	
	FREQUENCY	AREA (m^2)	FREQUENCY	AREA (m^2)
debris slide	108	58,313	106	118,144
debris slides/debris flow	25	41,353	54	177,443
channelized flow erosion	8	27,598	1	432
TOTAL	141	127,264	161	296,019

4.2. IC statistics

Statistics of the IC values calculated for each type of instability process (i.e., sediment source) are summarized within the violin plots in Fig. 9 and in the Table 6. The plots show that the minimum and median IC, as well as the density distribution, are higher in areas affected by DS/DF than in those affected by DS and CFE. The highest IC values are associated to DS closest to the target. The lowest IC values are associated to DS in the upper part of the catchments, mainly in the upper west catchment.

Fig. 10 presents a scatterplot of the relationship between average IC calculated for each polygon and the distance from the target. As expected, IC tends to increase approaching the target but a large variability of IC values of sediment sources at the same distance from the target can be observed. Average IC of debris slides spans from −4.29 to 0.44 due to the occurrence of such processes from divides to the valley bottoms, throughout areas with different magnitudes of the IC. In the same plot of Fig. 10, the relatively highest connectivity of DS/DF compared to the other processes is also evident, even at highest distances (e.g., more than 2000 m).

Specific differences can be identified between the processes that occurred in the two catchments, as reported in the box plots of Fig. 11. In particular, all the medians of the average IC are higher for the east catchment (DS = −3.05; DS/DF = −2.81; CFE = −2.86) compared to the

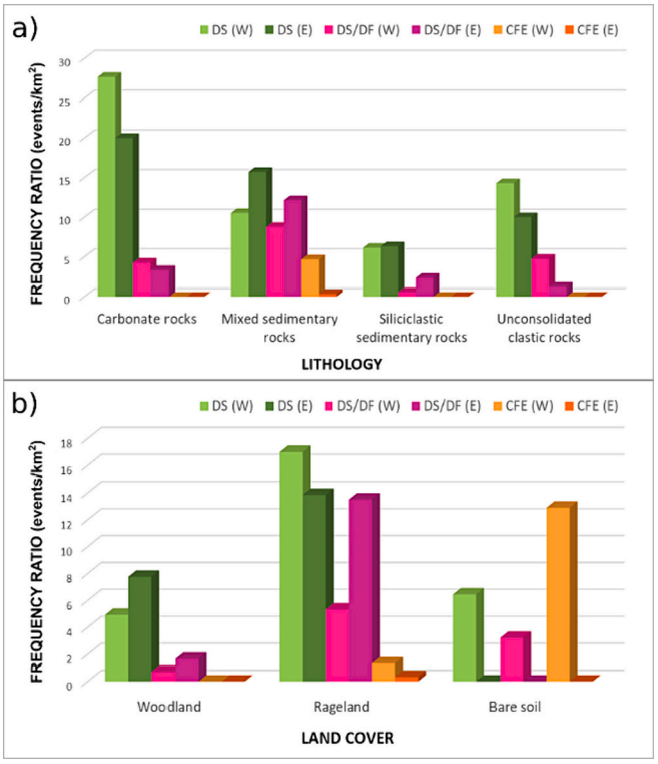

Fig. 7. Distribution of debris slide, debris slide/debris flow and channelized flow erosion with respect to the lithological (a) and land cover classes (b).

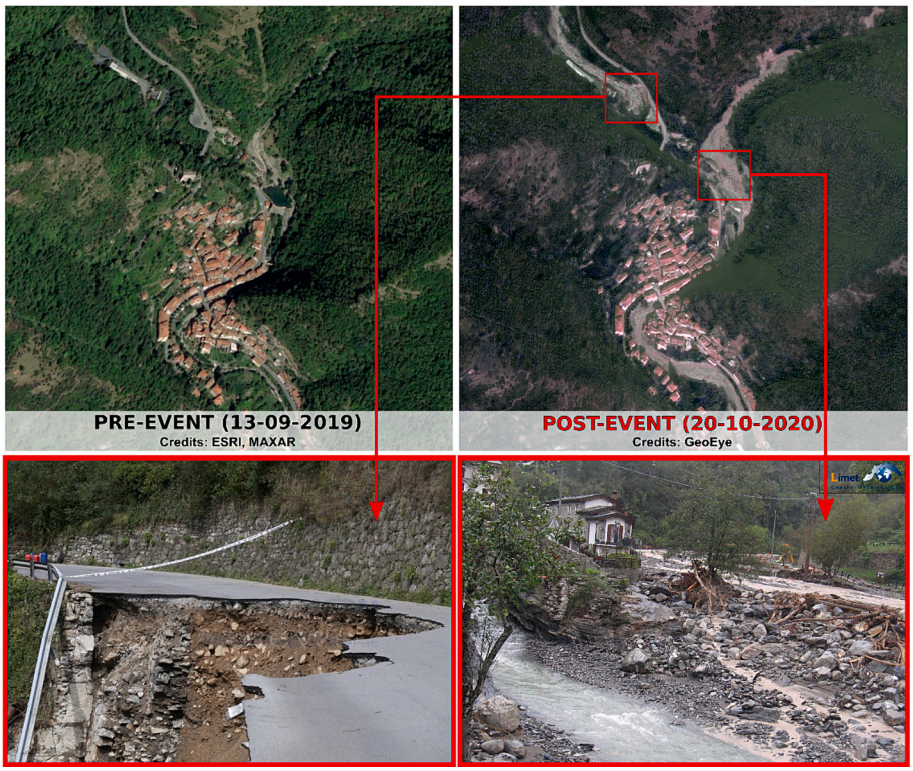

Fig. 6. VHR images of the outlet zone at Molini di Triora Village. The two aerial pictures namely "pre-event" and "post-event" show the relevant deposition. The two pictures below show examples of landslide caused by the undercutting of the slope by turbulent flows (on the left), and massive deposition with bank erosion (on the right).

Table 4
Frequency of instability processes according to land cover and lithology.

Land cover	Frequency					
	debris slides		debris slides/debris flows		channelized flow erosion	
Catchment	W	E	W	E	W	E
Woodland	55	65	8	14	0	0
Rangeland	51	41	16	40	4	1
Bare soil	2	0	1	0	4	0

Lithology	Frequency					
	debris slides		debris slides/ debris flows		channelized flow erosion	
Catchment	W	E	W	E	W	E
Carbonate rocks	13	6	2	1	0	0
Mixed sedimentary rocks	18	44	15	34	8	1
Siliciclastic sedimentary rocks	74	48	7	18	0	0
Unconsolidated clastic rocks	3	8	1	1	0	0

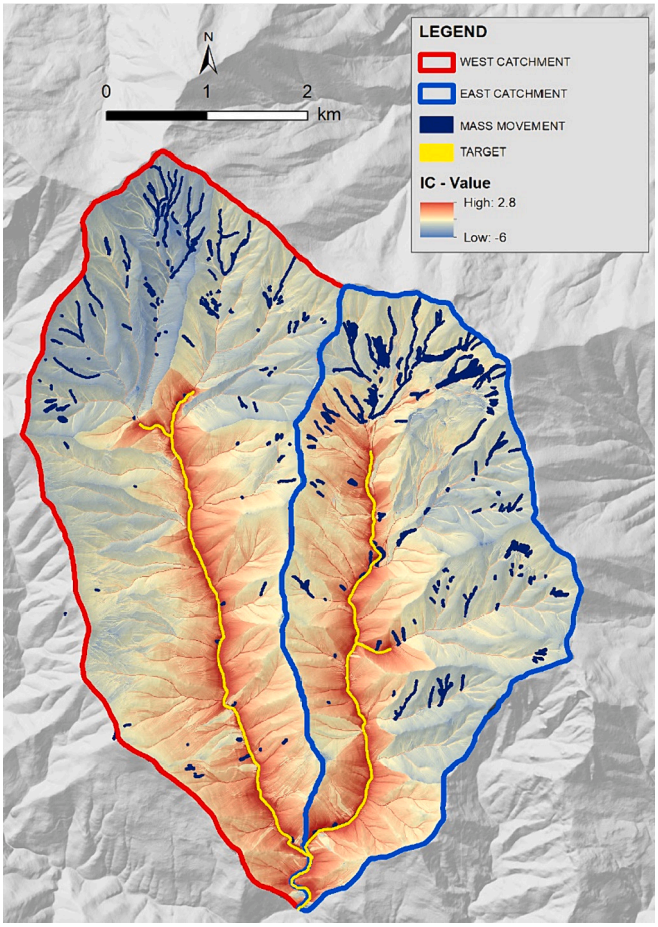

Fig. 8. Map of the Index of Connectivity with the inventoried mass movements.

Table 5
Statistics of the Index of Connectivity for the two catchments.

Catchment	IC MIN	IC MAX	IC RANGE	IC MEAN	IC STD
WEST	−5.9	2.8	8.7	−2.8	0.78
EAST	−5.8	2.8	8.6	−2.7	0.72

west catchment (DS = −3.60; DS/DF = −3.38; CFE = −3.61). It is worth noting that DS/DF are characterized by the highest median value and, similarly to the previous statistics, such processes show the highest

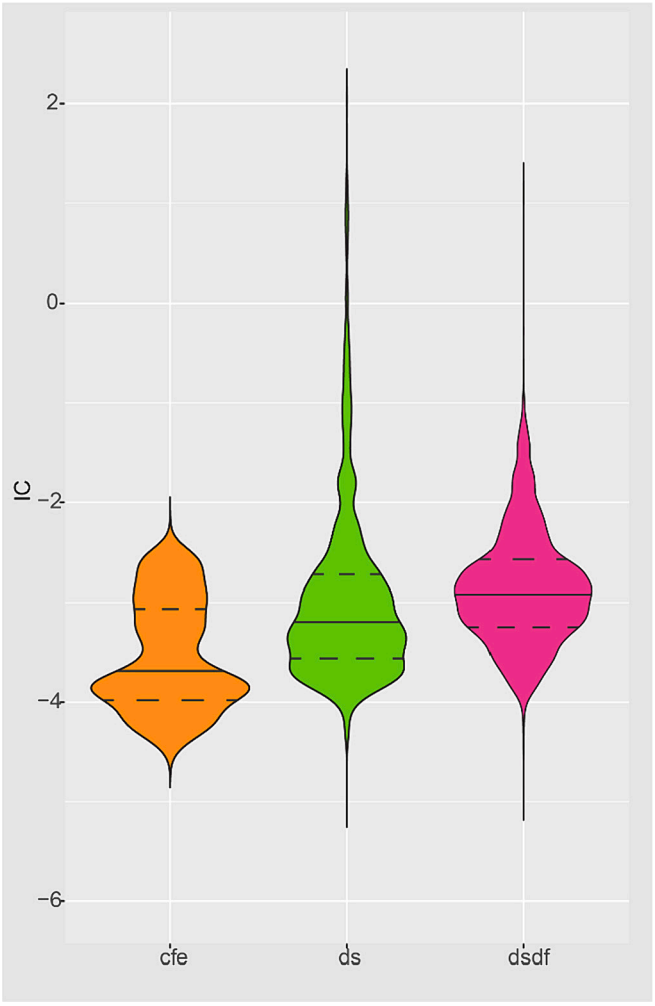

Fig. 9. Violin plot of the index of connectivity based on the three types of mass movement. The black lines indicate median values (50th percentile); the dashed lines indicate interquartile range (25th and 75th percentiles).

Table 6
Statistics of the Index of Connectivity for each type of instability process.

PROCESS	IC MIN	IC 5 %	IC 50 %	IC 95 %	IC MAX
DS/DF	−4.96	−3.69	−2.91	−1.75	1.19
DS	−4.97	−3.85	−3.19	−1.08	2.06
CFE	−4.49	−4.28	−3.72	−2.55	−2.31

average IC values in both catchments, with respect to the other processes. In addition, DS/DF are characterized also by the highest elongation (Fig. 12), with values up to 19. In the east catchment, this property is coupled with larger affected areas (see circles indicating areas higher than 10,000 m^2) and higher IC values ranging between −3 and − 1.

4.3. Geomorphological Landslide Inventory Map (GLIM) and IC comparison

The total area covered by the geomorphological landslide inventory map (GLIM) shown in Fig. 13 is 8.9×10^6 m^2. In particular, the GLIM covers an area of 3.9×10^6 m^2 in the east catchment and an area of 5.05×10^6 m^2 in the west catchment. The mapped landslides are of both slide and flow types. The largest mapped landslides occur in the middle portion of the west catchment (1.4×10^6 m^2) and in the upper part of the east catchment (1.38×10^6 m^2). The related deposits reactivated

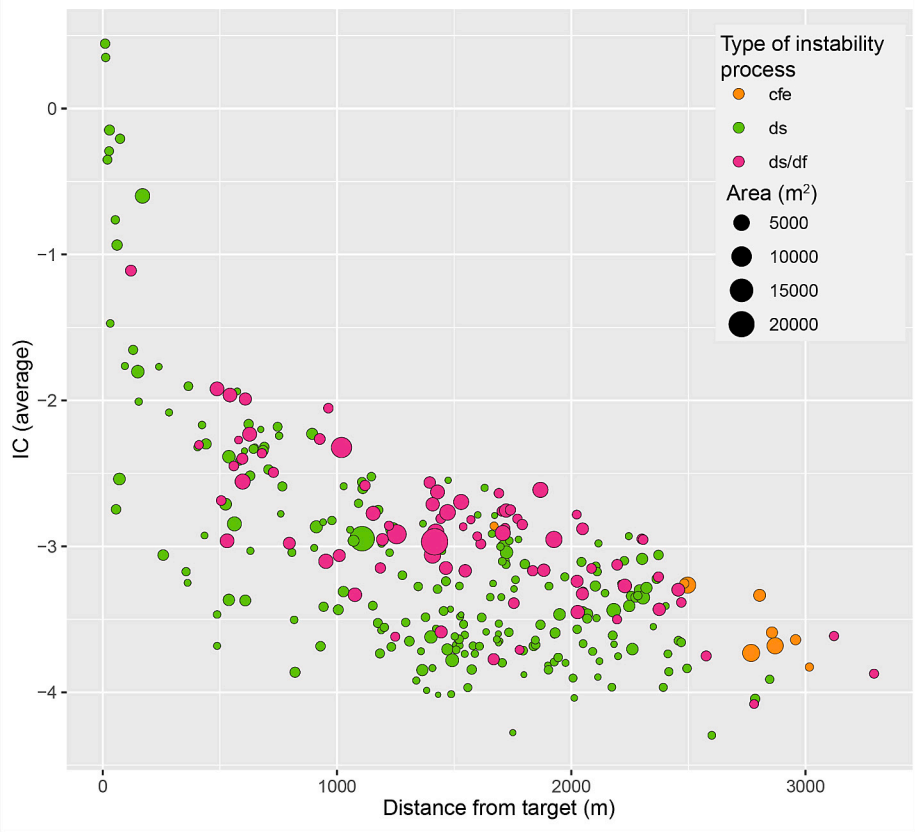

Fig. 10. Plot of the average IC versus distance from target. Different colors mean different types of mass movement. The size of the symbols indicates the area of the features.

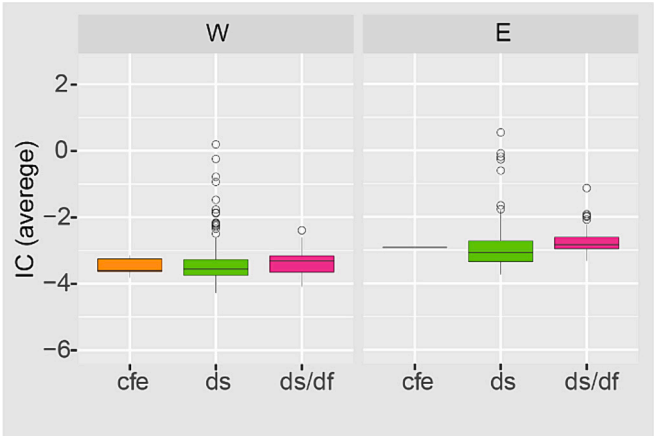

Fig. 11. Box plots of the average IC calculated according to the three types of mass movement, in the west (W) and east (E) catchments.

through time resulting in secondary generations of mass movements (Fig. 13).

In order to investigate the legacy effects, we analyzed the spatial relationships between landslides inventoried in the GLIM and instabilities triggered by the storm Alex contained in the event landslide inventory map (ELIM) described in the Section 4.1. The probability density chart in Fig. 14a shows that for areas higher than 1000 m^2, the ELIM polygons intersecting the GLIM are larger compared to those that do not intersect GLIM. Most of the ELIM processes in the west catchement occurred in areas not affected by those of GLIM (97 vs 45 in Table 7). On the other side, most of the ELIM in the East catchment

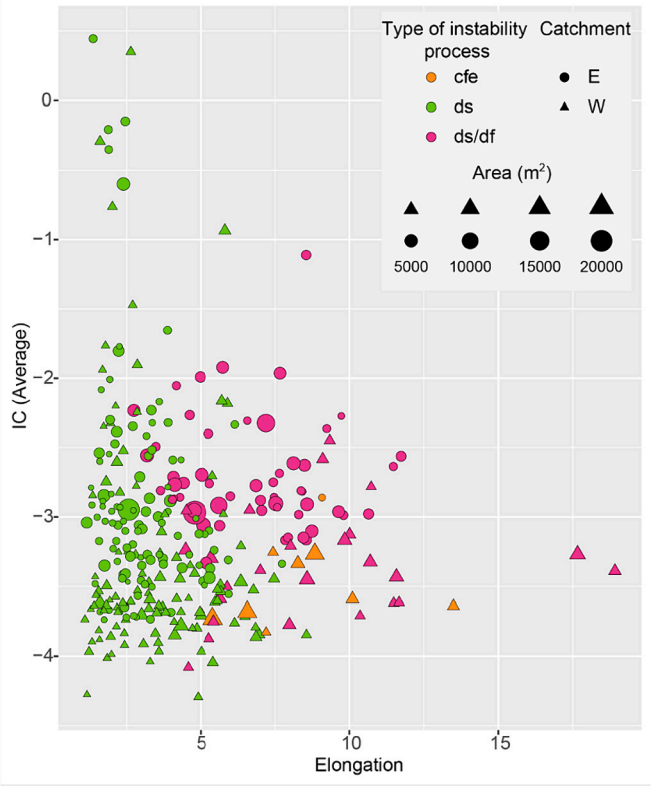

Fig. 12. Plot of the average IC versus elongation of the three types of mass movement.

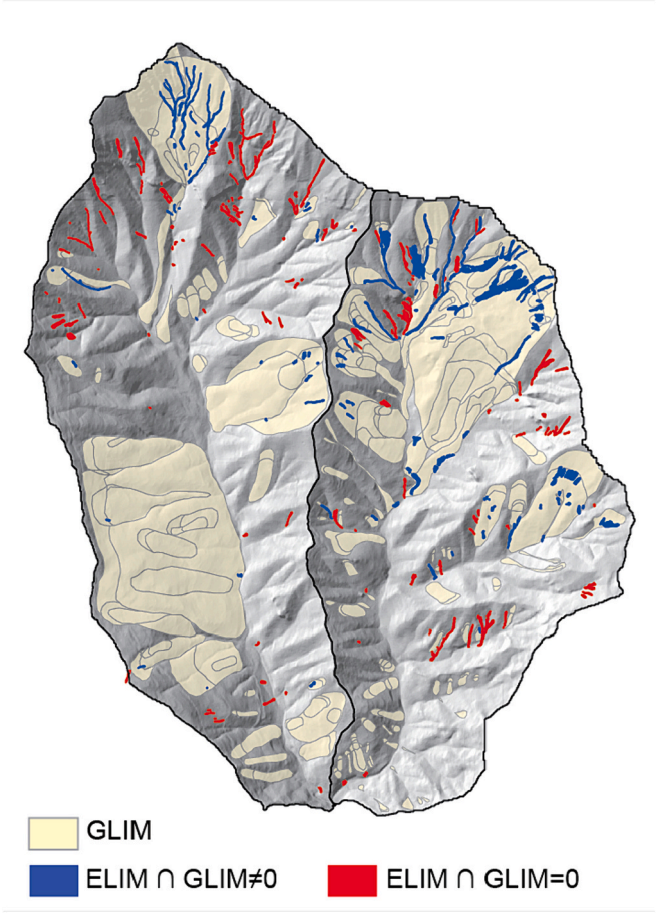

Fig. 13. Geomorphological Landslide inventory map (GLIM) and storm Alex-related ELIM processes. Blue polygons are the ELIM intersecting the GLIM processes; red polygons are the ELIM processes in areas not affected by GLIM.

occurred within areas affected by GLIM (94 vs 67 in Table 7).

The average IC was also calculated within the ELIM polygons intersecting the GLIM ones, as well as within those which do not intersect the GLIM. Generally, the probability density in Fig. 14b reveals that the former are more connected compared to the others. However, the average IC value of the ELIM intersecting GLIM in the west catchment (-3.28 ± 0.73) is lower compared to the ELIM intersecting GLIM in the east catchment (-2.85 ± 0.67), in accordance with the other statistics shown in Table 7. This demonstrates slightly higher connectivity conditions in the east catchment.

5. Discussion

A displacement of large amounts of sediment has been recognized frequently in mountain catchments hit by extreme rainfall events. In many cases, however, post-event surveys have been concentrated in urban areas affected by severe damage or loss of lives downstream, without specific assessments of sediment source areas up in the catchments. The identification of such areas is crucial for evaluating the residual risk, as well as for planning prevention measures aimed at reducing the amount of sediments which could inundate the same urban centers in the future. In addition, the acquisition of information about the ground effects immediately after an intense or extreme rainfall event similar to the one here described is essential also for analyzing the sediment cascade. Generally, one of the reasons that hampers this activity is the lack of experts that should operate in the field or by means of remote sensing technologies, soon after the events. In the current case study, availability of VHR satellite images taken on 20 October 2020 (less than 20 days after the occurrence of storm Alex) allowed the preparation of an event landslide inventory map ELIM (Ardizzone et al., 2012; Ardizzone et al., 2007) in two small catchments located in the highest part (at the divide) of the territory hit by the storm. The research outcomes described in the previous sections highlight that the different datasets indicated into the Section 3.1 were all necessary to understand location, magnitude and typologies of mass movements, and to create the event inventory map (Fig. 5). But, at the same time, these datasets

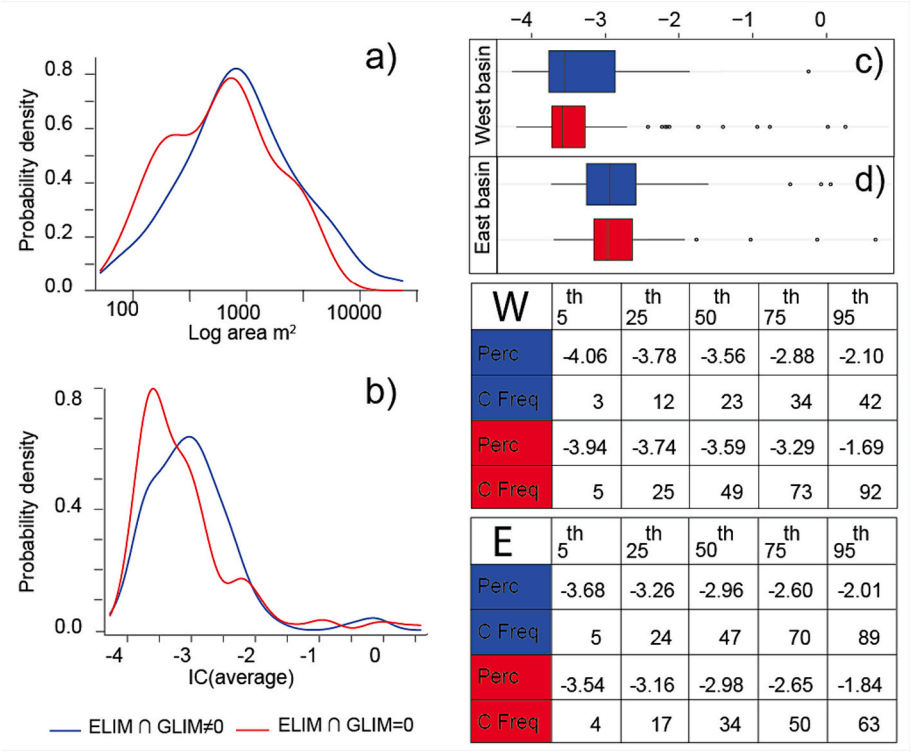

W	th 5	th 25	th 50	th 75	th 95
Perc	-4.06	-3.78	-3.56	-2.88	-2.10
C Freq	3	12	23	34	42
Perc	-3.94	-3.74	-3.59	-3.29	-1.69
C Freq	5	25	49	73	92

E	th 5	th 25	th 50	th 75	th 95
Perc	-3.68	-3.26	-2.96	-2.60	-2.01
C Freq	5	24	47	70	89
Perc	-3.54	-3.16	-2.98	-2.65	-1.84
C Freq	4	17	34	50	63

Fig. 14. a) Probability density of the ELIM areas; b) probability density of the IC index (average value in the ELIM polygons); c) and d) box plots of the IC for the ELIM in the west and east catchments. Percentiles of IC and the relative cumulative frequency of ELIM are reported into the table.

Table 7
Statistics of the ELIM and GLIM processes (ELIM ∩ GLIM ≠ 0 means intersection - ELIM ∩ GLIM = 0 means not intersection).

	West catchment		East catchment	
	ELIM ∩ GLIM≠0	ELIM ∩ GLIM = 0	ELIM ∩ GLIM≠0	ELIM ∩ GLIM = 0
Number of landslides	45	97	94	67
Total event landslide area (m^2)	4.84 × 104	8.02 × 104	2.06 × 105	8.92 × 104
Avarege landslide area (m^2)	1074	826	2199	1331
IC average ± sd	−3.28 ± 0.73	−3.33 ± 0.78	−2.85 ± 0.67	−2.79 ± 0.75

were not sufficient to understand the sediment dynamics within the catchments and to comprehend sediment transfer to the outlet. This was also influenced by the use of VHR post-event images (GeoEye) affected by shadow effects that impeded us to observe the sediments pathways beyond the source areas, as well as to identify the specific processes which have supplied sediments to the outlet. In addition, we started to analyze this event when field surveys were no longer useful to assess this type of information. For this reason, the mapping activity was complemented with the analysis of the structural sediment connectivity that, as mentioned before, can explain the possible sediment transfer paths at the catchment scale. In the available literature, a few studies exploit the combined use of these two types of dataset (e.g., Yan et al., 2022; Spiekermann et al., 2022; Schopper et al., 2019) indicating the relevant potentialities of their coupling. In the study area, the integrated analysis of connectivity and landslide characteristics, such as size and typology, provided interesting information on sediment cascade within the catchment, as also observed by Yan et al. (2022). A greater contribution of the east catchment with respect to the western one in supplying sediments to the outlet was observed. Even though this latter statement

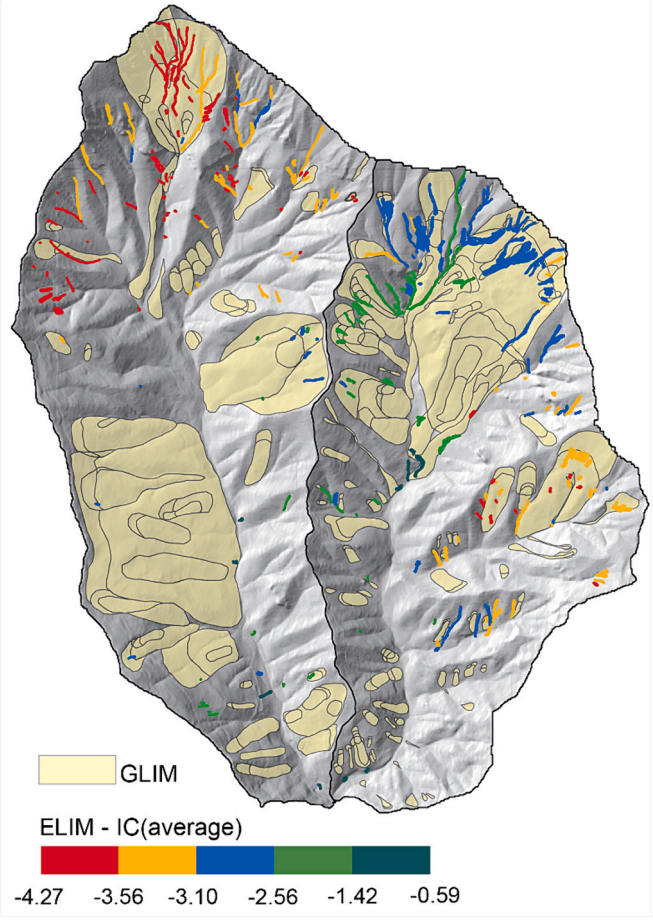

Fig. 15. GLIM and ELIM landslides coloured according to the average IC values.

cannot be confirmed by volumetric data, a reasonable evidence is provided by the map in Fig. 5 showing that most of the processes with long runout concentrated at the head of the east catchment where, according to the IC map (Fig. 8), hillslopes are more effectively connected to the target. The visual interpretation of the VHR GeoEye images allowed understanding that processes with long runout consisted of debris slides transitioned into debris flows downstream (Fig. 5), as also shown by elongation data reported in the plot of Fig. 12. In this plot, as well as in those reported in the Figs. from 9 to 11, it is worth noting that the DS/DF are associated with relatively higher connectivity than other typologies. Specifically, the violin plots in Fig. 9 show the highest median of the IC values related to the DS/DF, as well as a symmetrical kernel density compared to that positively skewed of the DS and CFE. This symmetry can be also related to the elongated and larger shape of the DS/DF (Fig. 12) allowing to intersect more variable IC values, depending on the spatial relationships with the target. On the other side, as expected, data in Fig. 10 highlight the highest IC values associated to the debris slides occurred close to the target as a consequence of local undercutting of the slopes. With regard to the target, the choice of delineating it along the valley bottoms by applying a constant buffer of 25 m to the main drainage channels was taken on the base of a substantial uniformity of the channel widths within the catchments. It is worth highlighting that variability of the channel network during a high magnitude event is surely an important aspect that deserves to be taken into account when conducting connectivity analyses. Given the predictive scope of our study, we decided to model a single scenario just considering the main channel network in the valley floors of the two catchments to provide a general portrait of lateral sediment connectivity patterns. Further studies could better investigate the dynamicity of sediment connectivity with varying channel networks generated from different magnitude events. Assessing the connectivity of each hillslope instability represents valuable information to prioritize structural interventions aimed at hazard reduction at the catchment scale. Therefore, besides a spatial characterization of sediment dynamics useful to understand the geomorphic systems' behavior, the planning of countermeasures can be considered among the most relevant and practical applications of the IC based on its predictive capability (Pellegrini et al., 2021; Martini et al., 2022). For this reason, novel approaches are being implemented to identify areas that are both susceptible to the initiation of mass movements and structurally connected to the main channel network (Spiekermann et al., 2022; Martini et al., 2022), where sediments can be delivered leading to severe damage to anthropic structures. In the light of this, Steger et al. (2022) pointed out as the combined use of susceptibility models with IC maps should be encouraged because areas which are structurally connected to a channel can be not prone to trigger a specific type of mass movement while, on the other side, large susceptible terrains may be disconnected from downslope channels. In the current case study, the IC information was coupled with an event-based inventory map and not with a susceptibility model. On one side, this represents a good basis to identify potential sources of sediment that were hazardous for settlements and infrastructures and may reactivate in the future. On the other side, this basis could be not sufficient for single events like the storm Alex characterized by a relevant variability of the rain in the space, leading to a weak density of mass movements in areas which are as much as susceptible and connected to generate damage downstream. Bordoni et al. (2018) also remarked that IC can be

used to improve susceptibility estimations and thus the predictive capability of identifying areas prone to damaging sediment transport processes.

The highest frequency of processes within the east catchment (Fig. 5; Table 3) can be reasonably attributed to the characteristics of the rainfall event. In fact, the comparison of the mapped instabilities with both land cover and lithological data of the two catchments does not suggest a control of these factors on the spatial concentration of the mapped processes (Fig. 7), neither morphometric properties show significant differences (Table 1). Accordingly, beginning on 02 October 2020, the rainfall increased towards the eastern direction concentrating mostly over the east catchment. As explained in the Section 2, this was confirmed by both data measured by rain gauges of the ARPAL network and by the ANTILOPE reanalyzed product (Fig. 3).

Analysis of the spatial relationships between the mapped mass failures and land cover (Fig. 7 and Table 4) shows the highest concentration of DS and DS/DF in the rangeland category, occurring mostly at the highest altitudes of the two catchments. A lower frequency ratio of these processes is instead observed in the woodland category. This finding is not surprising if one considers the well known role of vegetation in slope stabilization, that is typical of wooded areas. However, statistics highlight that debris slides are pretty frequent in the woodland category, demonstrating that the presence of trees with well developed root systems could be not sufficient in avoiding sliding processes.

The spatial distribution with respect to lithology (Fig. 7 and Table 4) is less clear compared to land cover. The DS/DF are more frequent in mixed sedimentary rocks, whereas DS occur mostly in carbonate rocks. The DS, however, result also frequent in unconsolidated clastic rocks that in the east catchment coincide with deposits of a deep-seated landslide mapped in this work (Fig. 13). In fact, the analysis of the relationships between ELIM and BLIM reveals that many of the event landslides exhibiting higher connectivity values developed within the depositional area of this larger pre-existing landslide located in the upper part of the eastern catchement. Although connectivity values are generally higher in the east catchment compared to the western one, upon detailed consideration, a visual inspection of data reported in Fig. 15 reveals that the higher IC values are concentrated in the head area of the east catchment, in correspondence of the large pre-existing landslide. In particular, this large landslide shows also evidences of recent activity (see the dataset at this link: https://egms.land.copernicus.eu/) which justifies its ability to represent a preferential sediment source to supply material within the selected target (i.e. valley bottom).

Analyses like this, based on the visual interpretation of VHR imagery, require long times to realize the inventory maps. This may seem anachronistic at the current time, where the use of artificial intelligence and automatic procedures is increasing also among the geoscience community for the detection and mapping of landslides (Esposito et al., 2020; Prakash et al., 2020, 2021; Meena et al., 2021; Qi et al., 2020). In our opinion, in order to reach suitable detection, spatial accuracy, and detailed geomorphological properties of event landslides, the mapping experience and attitudes of geomorphologists are still necessary. At the same time, this is true for validating results derived from the developing machine or deep learning processes.

We stress the importance of preparing landslide maps in mountain catchments characterized by valley bottoms occupied by human settlements. Assessing the connectivity of mountain catchments, coupled with the accurate and complete landslide mapping, helps to understand sediment dynamics and from which part of the catchment sediment can be mobilized, and the preferred transport routes which may interact with human structures downstream.

6. Conclusions

The storm Alex that in 2020 hit the Mediterranean Alps represented an extreme meteorological event triggering devastating floods and landslides in both Italy and France, with severe consequences for people and anthropic settlements. Similar events are continuing to impact the Mediterranean basin, and in particular the Italian territory (e.g., Emilia-Romagna in May 2023), highlighting the need to deepen scientific knowledge about sediment connectivity in the urbanized catchments. After the Storm Alex, a detailed inventory of rainfall-induced hillslope instability processes was prepared by means of the visual interpretation of VHR satellite imagery in two adjacent mountain catchments of the Liguria Region (northern Italy) impacted by intense rainfall. The inventory map included a total of 302 features classified in debris slide (214), debris slides/debris flow (79) and channelized flow erosion (9). The eastern catchment was affected by more processes with respect to the western one. This was mostly due to the rainfall distribution that, starting on 02 October 2020, increased towards the eastern direction as confirmed by data of both rain gauges of the ARPAL network and the ANTILOPE reanalyzed product, as well as to the presence of pre-existing and active landslides. The map of the Index of Connectivity of the two catchments allowed knowing the different degrees of linkage between the hillslopes and the valley bottoms, where part of the mobilized sediments travelled up to the outlet, inundating the urban center of Molini di Triora. Besides the higher connectivity of the head of the east catchment compared to the head of the western one, the current analysis revealed that the sediment sources characterized by a relatively higher connectivity corresponded to DS/DF in the east catchment. These processes were also those with the highest elongation and area (177,443 m^2), suggesting to be the most important sediment sources supplying sediments to the main stream channels.

This information represents a relevant step forward compared to traditional event inventory maps since, in this way, it was possible to determine both the sediment sources and transfer pathways. This relevant knowledge can allow thus to understand the geomorphic systems' behavior, as well as to prioritize structural interventions aimed at hazard reduction at the catchment scale, based on the predictive capability of the IC.

By taking into account that extreme precipitation associated to Alex-like extratropical cyclones (Ginesta et al., 2023) is projected to increase over some areas of the Mediterranean basin (González-Alemán et al., 2019; Reale et al., 2022), studies like this should be increased and improved to provide useful information to public bodies engaged in risk prevention activities and land planning. The use of more accurate topographic and land use datasets represents interesting perspectives, as well as a refinement of automatic techniques for landslides detection and mapping.

CRediT authorship contribution statement

Francesca Ardizzone: Data curation, Conceptualization. **Giuseppe Esposito:** Writing – review & editing, Writing – original draft, Visualization, Methodology, Formal analysis, Data curation. **Marco Cavalli:** Methodology, Formal analysis, Data curation. **Stefano Crema:** Methodology, Formal analysis, Data curation. **Federica Fiorucci:** Writing – review & editing, Methodology, Formal analysis, Data curation, Conceptualization.

Declaration of competing interest

The authors declare that they have no known competing financial interests or personal relationships that could have appeared to influence the work reported in this paper.

Data availability

Data will be made available on request.

Acknowledgments

We thank Mauro Cardinali for providing a fruitful support in the identification and mapping of pre-existing landslides in the analyzed catchments. We are also grateful to the Editor and three anaymous reviewers for their comments and suggestions that helped us to improve the whole manuscript.

References

Ardizzone, F., Cardinali, M., Galli, M., Guzzetti, F., Reichenbach, P., 2007. Identification and mapping of recent rainfall-induced landslides using elevation data collected by airborne Lidar. Nat. Hazards Earth Syst. Sci. 7, 637–650. https://doi.org/10.5194/nhess-7-637-2007.

Ardizzone, F., Basile, G., Cardinali, M., Casagli, N., Del Conte, S., Del Ventisette, C., Fiorucci, F., Garfagnoli, F., Gigli, G., Guzzetti, F., Iovine, G., Mondini, A.C., Moretti, S., Panebianco, M., Raspini, F., Reichenbach, P., Rossi, M., Tanteri, L., Terranova, O., 2012. Landslide inventory map for the Briga and the Giampilieri catchments, NE Sicily, Italy. J. Maps 8, 176–180. https://doi.org/10.1080/17445647.2012.694271.

Ardizzone, F., Bucci, F., Cardinali, M., Fiorucci, F., Pisano, L., Santangelo, M., Zumpano, V., 2023. Geomorphological landslide inventory map of the Daunia Apennines, southern Italy. Earth Syst. Sci. Data 15, 753–767. https://doi.org/10.5194/essd-15-753-2023.

Bertoldi, W., Zanoni, L., Tubino, M., 2010. Assessment of morphological changes induced by flow and flood pulses in a gravel bed braided river: the Tagliamento River (Italy). Geomorphology 114, 348–360. https://doi.org/10.1016/j.geomorph.2009.07.017.

Bookhagen, B., 2010. Appearance of extreme monsoonal rainfall events and their impact on erosion in the Himalaya. Geomat. Nat. Haz. Risk 1, 37–50. https://doi.org/10.1080/19475701003625737.

Bordoni, M., Persichillo, M.G., Meisina, C., Crema, S., Cavalli, M., Bartelletti, C., Galanti, Y., Barsanti, M., Giannecchini, R., D'Amato Avanzi, G., 2018. Estimation of the susceptibility of a road network to shallow landslides with the integration of the sediment connectivity. Nat. Hazards Earth Syst. Sci. 18, 1735–1758. https://doi.org/10.5194/nhess-18-1735-2018.

Borga, M., Stoffel, M., Marchi, L., Marra, F., Jakob, M., 2014. Hydrogeomorphic response to extreme rainfall in headwater systems: Flash floods and debris flows. J. Hydrol. 518, 194–205. https://doi.org/10.1016/j.jhydrol.2014.05.022.

Borselli, L., Cassi, P., Torri, D., 2008. Prolegomena to sediment and flow connectivity in the landscape: a GIS and field numerical assessment. CATENA 75, 268–277. https://doi.org/10.1016/j.catena.2008.07.006.

Bracken, L.J., Turnbull, L., Wainwright, J., Bogaart, P., 2015. Sediment connectivity: a framework for understanding sediment transfer at multiple scales: SEDIMENT CONNECTIVITY: SEDIMENT TRANSFER AT MULTIPLE SCALES. Earth Surf. Process. Landforms 40, 177–188. https://doi.org/10.1002/esp.3635.

Bucci, F., Santangelo, M., Fiorucci, F., Ardizzone, F., Giordan, D., Cignetti, M., Notti, D., Allasia, P., Godone, D., Lagomarsino, D., Pozzoli, A., Norelli, E., Cardinali, M., 2021. Geomorphologic landslide inventory by air photo interpretation of the High Agri Valley (Southern Italy). J. Maps 17, 376–388. https://doi.org/10.1080/17445647.2021.1943552.

Bucci, F., Santangelo, M., Fongo, L., Alvioli, M., Cardinali, M., Melelli, L., Marchesini, I., 2022. A new digital lithological map of Italy at the 1:100 000 scale for geomechanical modelling. Earth Syst. Sci. Data 14, 4129–4151. https://doi.org/10.5194/essd-14-4129-2022.

Burt, T., Allison, R.J., 2010. Sediment Cascades: An Integrated Approach. Wiley, Chichester.

Buter, A., Heckmann, T., Filisetti, L., Savi, S., Mao, L., Gems, B., Comiti, F., 2022. Effects of catchment characteristics and hydro-meteorological scenarios on sediment connectivity in glacierised catchments. Geomorphology 402, 108128. https://doi.org/10.1016/j.geomorph.2022.108128.

Cardinali, M., Antonini, G., Reichenbach, P., Guzzetti, F., 2001. Photo geological and landslide inventory map for the Upper Tiber River basin. Pubblication CNR GNDCI n. 2116, Scale 1:1,200,000.

Cavalli, M., Trevisani, S., Comiti, F., Marchi, L., 2013. Geomorphometric assessment of spatial sediment connectivity in small Alpine catchments. Geomorphology 188, 31–41. https://doi.org/10.1016/j.geomorph.2012.05.007.

Cavalli, M., Tarolli, P., Dalla Fontana, G., Marchi, L., 2016. Multi-temporal analysis of sediment source areas and sediment connectivity in the Rio Cordon catchment (Dolomites). ROL 39, 27–30. https://doi.org/10.3301/ROL.2016.39.

Cavalli, M., Vericat, D., Pereira, P., 2019. Mapping water and sediment connectivity. Sci. Total Environ. 673, 763–767. https://doi.org/10.1016/j.scitotenv.2019.04.071.

Chmiel, M., Godano, M., Piantini, M., Brigode, P., Gimbert, F., Bakker, M., Courboulex, F., Ampuero, J.-P., Rivet, D., Sladen, A., Ambrois, D., Chapuis, M., 2022. Brief communication: Seismological analysis of flood dynamics and hydrologically triggered earthquake swarms associated with Storm Alex. Nat. Hazards Earth Syst. Sci. 22, 1541–1558. https://doi.org/10.5194/nhess-22-1541-2022.

Chochon, R., Martin, N., Lebourg, T., Vidal, M., 2022. Analysis of Extreme Precipitation during the Mediterranean Event Associated with the Alex storm in the Alpes-Maritimes: Atmospheric Mechanisms and Resulting Rainfall. In: Gourbesville, P., Caignaert, G. (Eds.), Advances in Hydroinformatics. Springer Water. Springer Nature Singapore, Singapore, pp. 397–418. https://doi.org/10.1007/978-981-19-1600-7_26.

Cislaghi, A., Bischetti, G.B., 2019. Source areas, connectivity, and delivery rate of sediments in mountainous-forested hillslopes: A probabilistic approach. Sci. Total Environ. 652, 1168–1186. https://doi.org/10.1016/j.scitotenv.2018.10.318.

Crema, S., Cavalli, M., 2018. SedInConnect: a stand-alone, free and open source tool for the assessment of sediment connectivity. Comput. Geosci. 111, 39–45. https://doi.org/10.1016/j.cageo.2017.10.009.

Cruden, D.M., Varnes, D.J., 1996. Landslide types and processes. In: Turner, A.K., Shuster, R.L. (Eds.), Landslides: Investigation and Mitigation, Transportation Research Board, Special Report No. 247, pp. 36–75.

Cucchiaro, S., Cazorzi, F., Marchi, L., Crema, S., Beinat, A., Cavalli, M., 2019. Multi-temporal analysis of the role of check dams in a debris-flow channel: linking structural and functional connectivity. Geomorphology 345, 106844. https://doi.org/10.1016/j.geomorph.2019.106844.

Esposito, G., Marchesini, I., Mondini, A.C., Reichenbach, P., Rossi, M., Sterlacchini, S., 2020. A spaceborne SAR-based procedure to support the detection of landslides. Nat. Hazards Earth Syst. Sci. 20, 2379–2395. https://doi.org/10.5194/nhess-20-2379-2020.

Fiorucci, F., Cardinali, M., Carlà, R., Rossi, M., Mondini, A.C., Santurri, L., Ardizzone, F., Guzzetti, F., 2011. Seasonal landslide mapping and estimation of landslide mobilization rates using aerial and satellite images. Geomorphology 129, 59–70. https://doi.org/10.1016/j.geomorph.2011.01.013.

Fiorucci, F., Ardizzone, F., Mondini, A.C., Viero, A., Guzzetti, F., 2019. Visual interpretation of stereoscopic NDVI satellite images to map rainfall-induced landslides. Landslides 16, 165–174. https://doi.org/10.1007/s10346-018-1069-y.

Fressard, M., Cossart, E., 2019. A graph theory tool for assessing structural sediment connectivity: Development and application in the Mercurey vineyards (France). Sci. Total Environ. 651, 2566–2584. https://doi.org/10.1016/j.scitotenv.2018.10.158.

Fryirs, K., 2013. (Dis)Connectivity in catchment sediment cascades: a fresh look at the sediment delivery problem: (DIS)CONNECTIVITY IN CATCHMENT SEDIMENT CASCADES. Earth Surf. Process. Landforms 38, 30–46. https://doi.org/10.1002/esp.3242.

Fryirs, K.A., Brierley, G.J., Preston, N.J., Kasai, M., 2007. Buffers, barriers and blankets: the (dis)connectivity of catchment-scale sediment cascades. CATENA 70, 49–67. https://doi.org/10.1016/j.catena.2006.07.007.

Galli, M., Ardizzone, F., Cardinali, M., Guzzetti, F., Reichenbach, P., 2008. Comparing landslide inventory maps. Geomorphology 94, 268–289. https://doi.org/10.1016/j.geomorph.2006.09.023.

Ginesta, M., Yiou, P., Messori, G., Faranda, D., 2023. A methodology for attributing severe extratropical cyclones to climate change based on reanalysis data: the case study of storm Alex 2020. Climate Dynam. 61, 229–253. https://doi.org/10.1007/s00382-022-06565-x.

González-Alemán, J.J., Pascale, S., Gutierrez-Fernandez, J., Murakami, H., Gaertner, M. A., Vecchi, G.A., 2019. Potential increase in hazard from Mediterranean hurricane activity with global warming. Geophys. Res. Lett. 46, 1754–1764. https://doi.org/10.1029/2018GL081253.

Guzzetti, F., Mondini, A.C., Cardinali, M., Fiorucci, F., Santangelo, M., Chang, K.-T., 2012. Landslide inventory maps: New tools for an old problem. Earth-Science Reviews 112, 42–66. https://doi.org/10.1016/j.earscirev.2012.02.001.

Handwerger, A.L., Fielding, E.J., Huang, M., Bennett, G.L., Liang, C., Schulz, W.H., 2019. Widespread Initiation, Reactivation, and Acceleration of Landslides in the Northern California Coast Ranges due to Extreme Rainfall. Case Rep. Med. 124, 1782–1797. https://doi.org/10.1029/2019JF005035.

Harvey, A.M., 2002. Effective timescales of coupling within fluvial systems. Geomorphology 44, 175–201. https://doi.org/10.1016/S0169-555X(01)00174-X.

Heckmann, T., Cavalli, M., Cerdan, O., Foerster, S., Javaux, M., Lode, E., Smetanová, A., Vericat, D., Brardinoni, F., 2018. Indices of sediment connectivity: opportunities, challenges and limitations. Earth-Science Reviews 187, 77–108. https://doi.org/10.1016/j.earscirev.2018.08.004.

Keesstra, S., Nunes, J.P., Saco, P., Parsons, T., Poeppl, R., Masselink, R., Cerdà, A., 2018. The way forward: can connectivity be useful to design better measuring and modelling schemes for water and sediment dynamics? Sci. Total Environ. 644, 1557–1572. https://doi.org/10.1016/j.scitotenv.2018.06.342.

Martini, L., Picco, L., Iroumé, A., Cavalli, M., 2019. Sediment connectivity changes in an Andean catchment affected by volcanic eruption. Sci. Total Environ. 692, 1209–1222. https://doi.org/10.1016/j.scitotenv.2019.07.303.

Martini, L., Cavalli, M., Picco, L., 2022. Predicting sediment connectivity in a mountain basin: a quantitative analysis of the index of connectivity. Earth Surf Processes Landf 47, 1500–1513. https://doi.org/10.1002/esp.5331.

Meena, S.R., Ghorbanzadeh, O., Van Westen, C.J., Nachappa, T.G., Blaschke, T., Singh, R. P., Sarkar, R., 2021. Rapid mapping of landslides in the Western Ghats (India) triggered by 2018 extreme monsoon rainfall using a deep learning approach. Landslides 18, 1937–1950. https://doi.org/10.1007/s10346-020-01602-4.

Murillo-García, F., Rossi, M., Fiorucci, F., Alcántara-Ayala, I., 2015. Population Landslide Vulnerability Evaluation: The Case of the Indigenous Population of Pahuatlán-Puebla, Mexico. In: Lollino, G., Giordan, D., Crosta, G.B., Corominas, J., Azzam, R., Wasowski, J., Sciarra, N. (Eds.), Engineering Geology for Society and Territory - Volume 2. Springer International Publishing, Cham, pp. 1793–1797. https://doi.org/10.1007/978-3-319-09057-3_317.

Najafi, S., Dragovich, D., Heckmann, T., Sadeghi, S.H., 2021. Sediment connectivity concepts and approaches. CATENA 196, 104880. https://doi.org/10.1016/j.catena.2020.104880.

Passalacqua, P., Belmont, P., Staley, D.M., Simley, J.D., Arrowsmith, J.R., Bode, C.A., Crosby, C., DeLong, S.B., Glenn, N.F., Kelly, S.A., Lague, D., Sangireddy, H., Schaffrath, K., Tarboton, D.G., Wasklewicz, T., Wheaton, J.M., 2015. Analyzing high resolution topography for advancing the understanding of mass and energy transfer

through landscapes: a review. Earth Sci. Rev. 148, 174–193. https://doi.org/10.1016/j.earscirev.2015.05.012.
Pellegrini, G., Martini, L., Cavalli, M., Rainato, R., Cazorzi, A., Picco, L., 2021. The morphological response of the Tegnas alpine catchment (Northeast Italy) to a large Infrequent Disturbance. Sci. Total Environ. 770, 145209 https://doi.org/10.1016/j.scitotenv.2021.145209.
Peng, J., Fan, Z., Wu, D., Zhuang, J., Dai, F., Chen, W., Zhao, C., 2015. Heavy rainfall triggered loess–mudstone landslide and subsequent debris flow in Tianshui, China. Eng. Geol. 186, 79–90. https://doi.org/10.1016/j.enggeo.2014.08.015.
Persichillo, M.G., Bordoni, M., Cavalli, M., Crema, S., Meisina, C., 2018. The role of human activities on sediment connectivity of shallow landslides. CATENA 160, 261–274. https://doi.org/10.1016/j.catena.2017.09.025.
Prakash, N., Manconi, A., 2021. Rapid Mapping of Landslides Triggered by the Storm Alex, October 2020. In: 2021 IEEE International Geoscience and Remote Sensing Symposium IGARSS. Presented at the IGARSS 2021–2021 IEEE International Geoscience and Remote Sensing Symposium. IEEE, Brussels, Belgium, pp. 1808–1811. https://doi.org/10.1109/IGARSS47720.2021.9553321.
Prakash, N., Manconi, A., Loew, S., 2020. Mapping Landslides on EO Data: Performance of Deep Learning Models vs. Traditional Machine Learning Models. Remote Sensing, 12, p. 346. https://doi.org/10.3390/rs12030346.
Prakash, N., Manconi, A., Loew, S., 2021. A new strategy to map landslides with a generalized convolutional neural network. Sci. Rep. 11, 9722. https://doi.org/10.1038/s41598-021-89015-8.
Qi, W., Wei, M., Yang, W., Xu, C., Ma, C., 2020. Automatic Mapping of Landslides by the ResU-Net. Remote Sens. (Basel) 12, 2487. https://doi.org/10.3390/rs12152487.
Rainato, R., Mao, L., García-Rama, A., Picco, L., Cesca, M., Vianello, A., Preciso, E., Scussel, G.R., Lenzi, M.A., 2017. Three decades of monitoring in the Rio Cordon instrumented basin: Sediment budget and temporal trend of sediment yield. Geomorphology 291, 45–56. https://doi.org/10.1016/j.geomorph.2016.03.012.
Reale, M., Cabos Narvaez, W.D., Cavicchia, L., Conte, D., Coppola, E., Flaounas, E., Giorgi, F., Gualdi, S., Hochman, A., Li, L., Lionello, P., Podrascanin, Z., Salon, S., Sanchez-Gomez, E., Scoccimarro, E., Sein, D.V., Somot, S., 2022. Future projections of Mediterranean cyclone characteristics using the Med-CORDEX ensemble of coupled regional climate system models. Climate Dynam. 58, 2501–2524. https://doi.org/10.1007/s00382-021-06018-x.
Schopper, N., Mergili, M., Frigerio, S., Cavalli, M., Poeppl, R., 2019. Analysis of lateral sediment connectivity and its connection to debris flow intensity patterns at different return periods in the Fella River system in northeastern Italy. Sci. Total Environ. 658, 1586–1600. https://doi.org/10.1016/j.scitotenv.2018.12.288.
Scorpio, V., Cavalli, M., Steger, S., Crema, S., Marra, F., Zaramella, M., Borga, M., Marchi, L., Comiti, F., 2022. Storm characteristics dictate sediment dynamics and geomorphic changes in mountain channels: a case study in the Italian Alps. Geomorphology 403, 108173. https://doi.org/10.1016/j.geomorph.2022.108173.
Singh, M., Sinha, R., Tandon, S.K., 2021. Geomorphic connectivity and its application for understanding landscape complexities: a focus on the hydro-geomorphic systems of India. Earth Surf Processes Landf 46, 110–130. https://doi.org/10.1002/esp.4945.
Spiekermann, R.I., Smith, H.G., McColl, S., Burkitt, L., Fuller, I.C., 2022. Development of a morphometric connectivity model to mitigate sediment derived from storm-driven shallow landslides. Ecol. Eng. 180, 106676 https://doi.org/10.1016/j.ecoleng.2022.106676.
Steger, S., Scorpio, V., Comiti, F., Cavalli, M., 2022. Data-driven modelling of joint debris flow release susceptibility and connectivity. Earth Surf Processes Landf. https://doi.org/10.1002/esp.5421 esp.5421.
Stoffel, M., Mendlik, T., Schneuwly-Bollschweiler, M., Gobiet, A., 2014. Possible impacts of climate change on debris-flow activity in the Swiss Alps. Clim. Change 122, 141–155. https://doi.org/10.1007/s10584-013-0993-z.
Surian, N., Righini, M., Lucía, A., Nardi, L., Amponsah, W., Benvenuti, M., Borga, M., Cavalli, M., Comiti, F., Marchi, L., Rinaldi, M., Viero, A., 2016. Channel response to extreme floods: Insights on controlling factors from six mountain rivers in northern Apennines, Italy. Geomorphology 272, 78–91. https://doi.org/10.1016/j.geomorph.2016.02.002.
Tarquini, S., Isola, I., Favalli, M., Battistini, A., Dotta, G., 2023. TINITALY, a digital elevation model of Italy with a 10 meters cell size (Version 1.1). Doi:10.13127/TINITALY/1.1.
Tiranti, D., Crema, S., Cavalli, M., Deangeli, C., 2018. An Integrated Study to Evaluate Debris Flow Hazard in Alpine Environment. Front. Earth Sci. 6, 60. https://doi.org/10.3389/feart.2018.00060.
Trevisani, S., Cavalli, M., 2016. Topography-based flow-directional roughness: potential and challenges. Earth Surf. Dynam. 4, 343–358. https://doi.org/10.5194/esurf-4-343-2016.
Wainwright, J., Turnbull, L., Ibrahim, T.G., Lexartza-Artza, I., Thornton, S.F., Brazier, R. E., 2011. Linking environmental régimes, space and time: Interpretations of structural and functional connectivity. Geomorphology 126, 387–404. https://doi.org/10.1016/j.geomorph.2010.07.027.
Yan, X., Jiao, J., Li, M., Qi, H., Liang, Y., Xu, Q., Zhang, Ziqi, Jiang, X., Li, J., Zhang, Zhixin, Wang, H., 2022. Lateral sediment connectivity of landslides occurred under a heavy rainstorm and its influence on sediment yield of slope-channel cascade on the Loess Plateau. CATENA 216, 106378. https://doi.org/10.1016/j.catena.2022.106378.
Yassine, R., Lastes, M., Argence, A., Gandouin, A., Imperatrice, C., Michel, P., Zhang, R., Brigode, P., Delestre, O., Taccone, F., 2022. Simulation of the Alex storm Flash-Flood in the Vésubie Catchment (South Eastern France) using Telemac-2D Hydraulic Code. In: Gourbesville, P., Caignaert, G. (Eds.), Advances in Hydroinformatics. Springer Water. Springer Nature Singapore, Singapore, pp. 847–863. https://doi.org/10.1007/978-981-19-1600-7_52.
Zanandrea, F., Michel, G.P., Kobiyama, M., 2020. Impedance influence on the index of sediment connectivity in a forested mountainous catchment. Geomorphology 351, 106962. https://doi.org/10.1016/j.geomorph.2019.106962.